Reduced mixing time in stirred vessels by means of irregular impellers

S. Başbuğ, G. Papadakis and J. C. Vassilicos
Department of Aeronautics, Imperial College London, SW7 2AZ London, UK

Abstract

Previous research[1,2] has shown that using fractal-like blades instead of regular ones can result in a significant decrease in the power consumption of an unbaffled stirred vessel with a four-bladed radial impeller. In order to fully assess the mixing efficiency of a fractal-like or just irregular impeller with respect to a regular impeller, the mixing time required to homogenize an injected passive scalar was evaluated for both impeller types at $Re = 320$ and 1600 using direct numerical simulations. It was observed that the irregular impeller can lead to a considerably shorter mixing time. This result was explained by the differences in characteristics of flow and scalar fields generated by the two impellers. We also assess the effect of Re in the transitional regime. Moreover, a simple mathematical model is proposed which can approximate the decay rate of the passive scalar fluctuations integrated over the tank volume.

I. Introduction

A. Fractal/multiscale generated flows

In the past decade, fundamental properties of flows generated by fractal/multiscale objects have been studied in detail.[3–8] These objects are created by repeating a geometrical pattern (e.g. a square grid-element) by decreasing the size of the pattern at every iteration. Further studies have demonstrated the benefits of fractal/multiscale objects in practical applications, such as the noise reduction,[9] vortex shedding suppression,[10–12] heat transfer enhancement[13] and flame control,[14–16] to name a few.

Suzuki et al.[17] investigated turbulent mixing of dye in a water channel in the wake of the regular and fractal grids that have the same blockage ratio (ratio of the area blocked by the grid to the channel cross-section). Experiments were conducted at a high Schmidt number, $Sc \approx 2100$, where $Sc = \nu/\Gamma$ is based on the kinematic viscosity of water (ν) and the molecular diffusivity (Γ) of dye in water. At the inlet of the channel, they imposed a step profile for the passive scalar (dye concentration) and assessed the vertical profiles of the mean scalar and scalar variance in the lee of the grids. Their results showed that mixing is enhanced when the fractal grid was used instead of the regular grid. The same conclusion was drawn in a computational study[18] with direct numerical simulations (DNS) using the same two grids as the aforementioned experimental work, but this time at a low Schmidt number, $Sc = 0.71$.

The DNS study of Laizet and Vassilicos[19] also compared the turbulent flow in the wake of a regular and fractal grid of equal blockage ratio. They imposed a constant scalar gradient normal to the mean flow direction at the inlet of the virtual wind tunnel and set $Sc = 0.1$. They observed that the turbulent transfer of scalar fluctuations in the direction of the scalar gradient is larger for the fractal than the regular grid by an order of magnitude downstream of the grids for the majority of the domain examined. The authors linked this improvement to the interaction of wakes of different sizes, since the fractal grid is composed of square grid-elements of different side lengths and bar thicknesses. Hence, they suggested that fractal objects can be employed to design energy-efficient industrial mixers

and heat transfer devices. This conclusion was further elaborated by the same authors in another study[20] where they compared three regular and three fractal grid designs, along with varying Sc and mean scalar gradients. In agreement with the previous study, it was observed that the transverse flux of turbulent scalar fluctuations was larger by an order of magnitude in the wake of all types of fractal grids investigated, compared to the regular ones.

B. Fractal impellers in stirred vessels

The outcomes summarized above motivated the utilization of fractal-like/multiscale geometries in stirred vessels. These mixing devices are employed in a wide range of applications in the chemical, pharmaceutical and process industries.[21] Steiros et al.[1] and Başbuğ et al.[2] introduced fractal impeller blades created with a modification of the regular, rectangular-shaped impeller blades. The design of the novel fractal blades was inspired by the fractal plates tested in wind tunnel experiments by Nedić et al.[22] who demonstrated that fractal plates generate higher turbulence intensity in their wake compared to square plates. Steiros et al.[1] measured the shaft torque of four-bladed radial impellers equipped with regular and fractal-like blades of equal frontal area, in an unbaffled stirred vessel at $Re = 1 - 2 \times 10^5$, where $Re = ND^2/\nu$ based on the rotational speed (N) and impeller diameter (D). They observed that the impeller with fractal-like blades has $11 - 12\%$ lower shaft torque, hence lower power consumption, compared to the impeller with the regular blades. Figure 1c (top) shows a sketch of one the two fractal-like blade shapes used by Steiros et al.[1], the other one being similar but with a second iteration of identically shaped but smaller irregularities superimposed on the irregular blade shown in Figure 1c. Their two-iterations fractal-like blade returned lower power consumption than both the one-iteration fractal-like (or just irregular) blade and the regular one.

DNS studies of Başbuğ et al.[2] compared the same regular and one-iteration fractal-like (or just irregular) blades used in the aforementioned experimental study, but in the transitional regime to make computations affordable. It was found that the irregular blade still results in a reduction of the impeller power at $Re = 1600$ by 8% compared to the

regular ones, whereas no difference was observed at $Re = 320$. The physical explanation of the reduction in the impeller torque and power consumption at $Re = 1600$, was provided by Başbuğ et al.[23] by comparing the DNS results of the flow fields generated by both impeller types. In order to determine whether this decrease in power consumption can potentially lead to an improvement in the process efficiency, the mixing performance of the irregular (one-iteration fractal-like) impeller must be also evaluated.

C. Mixing time in stirred vessels

Stirred tanks are employed for suspending solids or dispersing gas in liquids, blending of miscible liquids, creating immiscible liquid-liquid dispersions, and also for heating/cooling mixtures.[24] Mixing of a passive scalar has been the focus of a large number of studies for fundamental research purposes.[25–29] A passive scalar is transported by the flow, but does not react back, i.e. it does not affect the flow field in any dynamical sense. In order to evaluate the mixing performance of a stirred vessel, it is common practice to inject a passive scalar and measure the time required for its homogenization. This is especially suitable for predicting the blending time of miscible liquids, or for the study of heat transfer applications, since these cases do not involve a phase interface. Mixing operations are performed in the turbulent, transitional or laminar regime, mainly depending on the viscosity of the fluid, since this can be as low as e.g. $10^{-3}\,Pa \cdot s$ for water or as high as e.g. $150\,Pa \cdot s$ for corn syrup.[24] According to *Handbook of Industrial Mixing*, among these regimes the most limited understanding is for transitional regime.[24]

Turbulent flow is preferred for industrial processes due to its ability to transport and mix more effectively.[30] The scales of segregation are reduced by the turbulent eddies.[31] In a fully turbulent flow at high Re, the nondimensional parameters converge to a constant value. For instance, it is established that the nondimensional mixing time (normalized with the period of the impeller rotation, henceforth called t_{mix}) and the power number (defined as $\langle N_p \rangle = \langle P \rangle / (\rho N^3 D^5)$, where P is the power input and angular brackets $\langle\rangle$ represent the time-averaging operation) are constant for a given geometry.[21,32,33] The mean[34] and fluctuating[35] velocity profiles collapse in fully turbulent regime regardless of

Re, when normalized with the blade tip speed. Engineers benefit from these aspects of fully turbulent flows when a stirred vessel design needs to be scaled up or down.[24]

The literature regarding the estimation of mixing times of passive scalars in stirred vessels is dominated by studies conducted with baffled tanks operating at the turbulent regime. There are both experimental[36–44] and numerical studies available. Almost all of the numerical investigations used turbulence modelling, such as Reynold's averaged Navier-Stokes (RANS) models,[45–49] large eddy simulations (LES)[50–53] or detached eddy simulations (DES).[54] DES is based on LES, but uses a RANS model near the walls to avoid the high resolution required by LES in this region.

Pivotal experimental studies from 50's onwards[36–39] endeavoured to develop empirical correlations or scaling laws for the mixing time and required energy. The most extensive investigation is perhaps that of Grenville.[40] He performed a series of experiments in a baffled tank stirred with four-bladed flat and pitched blade turbines, using an electrolyte tracer for conductivity measurements at three probe points, for Re values in the range $200 < Re < 5 \times 10^4$. The obtained mixing times based on different probe points agreed well in the turbulent regime, whereas they varied significantly in the transient regime and the longest time was measured at the probe behind a baffle. For the turbulent regime and a tank with equal height and diameter, the following correlation was developed to estimate the mixing time: $t_{mix} = 5.2 \langle N_p \rangle^{-1/3} (T/D)^2$, where T and D are the diameters of the tank and impeller, respectively. Since then, this correlation was cited repeatedly by other sources.[24,33,51,55,56] For the transitional regime, the suggested correlation was: $t_{mix} = 183^2 \langle N_p \rangle^{-2/3} Re^{-1} (T/D)^2$. The surprising implication of these correlations was that the impellers with equal T/D and $\langle N_p \rangle$ would result in the same t_{mix}, irrespective of the impeller type and regardless of the geometric parameters other than T/D.[24] The interpretation was that the mean rate of the energy dissipation inside the tank determines t_{mix}.[24,33] The value of Sc was not mentioned in this report. Using the available data[40,57] we can estimate that Sc was $O(10^5)$ for the cases at the lowest Re considered, and it declined to $O(10^3)$ as Re was increased, due to the decreased fluid viscosity. Therefore, Pe was always $O(10^7)$, meaning that the diffusion was very slow compared to advection.

Some experimental studies used an unbaffled tank with an open surface, which leads to surface depression due to the highly swirling motion of the fluid.[42–44] Rousseaux et al.[42] suggested that the injection into the forced vortex zone was favourable for the fast mixing of the reagents and the consequent chemical reaction. Cabaret et al.[44] measured the power and the mixing time of eight different types of impellers in an unbaffled vessel. They observed that $\langle N_p \rangle$ scales with Re^{-a}, with $a = 1$ for $Re < 10$ and equal for all impellers types, whereas $a < 1$ for $10 < Re < 400$ and different for all impeller types. Moreover, all impeller types exhibited a decreasing trend of t_{mix} against Re for $10 < Re < 40$, but Sc was not stated. Assirelli et al.[43] compared the performance of a vessel under baffled and unbaffled conditions. Having the same power consumption, which was realised using different impeller speeds, the unbaffled tank delivered either a higher mixing efficiency than the baffled tank, or equal efficiency, depending on the injection location. However, the maximum achievable power of an unbaffled tank was limited by the surface vortex reaching the impeller and the consequent mechanical damage.

The introduction of RANS models provided a faster and cheaper tool than experimental methods, whereby all scales of turbulence are modelled. For the study of mixing in stirred vessels, the k-ϵ model was most widely used.[45–49] When the eddy viscosity (ν_t) was computed with a turbulence model, the turbulent Schmidt number ($Sc_t = \nu_t/\Gamma_t$) was used to predict the eddy diffusivity Γ_t. Sc_t can be based on experience or determined with trial and error.[47] Montante et al.[47] showed that the choice of Sc_t was critically important in order to get correct results of the mixing processes when the k-ϵ model was used. The value giving the best agreement with experiments, could also depend on the grid resolution of the simulation.[49] Although the k-ϵ model could predict the mean velocity profiles with reasonable success, the results on the mixing processes were deemed unreliable.[50,51]

In the LES approach, only the influence of smallest eddies (smaller than a predefined filter size) are modelled and large eddies are directly resolved in space and time.[30] LES studies of the flow field in stirred vessels were already published in mid 90's, first by Eggels,[58] then by Derksen and van den Akker.[59,60] It took almost ten more years until Yeoh et al.[50] employed this method for the assessment of t_{mix} in a stirred tank and

compared this against experimental results and empirical correlations. In order to estimate t_{mix}, they took the entire scalar field inside the tank into account, instead of using probe points. They reported that the discrepancies with respect to the references they compared their results with, varied between 9% and 53%, with an average of 18%. They observed that any estimate of t_{mix} using a single probe point would vary significantly across the vessel, leading to less realistic results. The discrepancies were attributed to this limitation, since experiments evaluated only a number of locations.

Hartmann et al.[51] also used the LES method to estimate t_{mix} in a baffled tank stirred with a Rushton turbine. They positioned the monitoring points in accordance to the experiments of Distelhoff et al.[41] and the numerical results agreed within 30% with the measured values. Yang et al.[54] assessed a possible improvement of the mixing efficiency of a stirred tank using the DES approach. They compared the performance of pitched blade turbines with centrically and eccentrically (radially shifted) located shafts in an unbaffled tank. They used 15 monitoring points to determine t_{mix}. The predictions matched with the experimental results obtained at the same locations to within 20%. Moreover, they reported a significant decrease in t_{mix} thanks to the eccentricity of the shaft, but did not report on the change in the power consumption due to this modification.

All aforementioned LES and DES studies used an injection of a passive scalar to investigate the mixing process, but employed different criteria to determine the time for the complete homogenization. The selected values of Sc_t varied between 0.7 and 0.8. Although LES is the most reliable numerical approach for high Re considering the available computational resources, it still requires the selection of a suitable value for Sc_t and it is not yet proven to provide an excellent agreement with experiments regarding the estimation of t_{mix}.

Derksen[56,61] performed DNS of the flow in a baffled tank stirred with a pitched blade turbine, and investigated the blending process of two miscible fluids, that is governed by the same set of equations as the mixing of a passive scalar. The author assessed the influences on t_{mix} stemming from the density differences[56] and viscosity differences[61] of the two fluids, at $Re = 3000, 6000$ and 12000, and $Sc = 1000$. The simulations were initiated

with the tank having the upper and lower halves filled with the two different fluids. Although the flow field was resolved almost down to the smallest scale (i.e. Kolmogorov length scale, η_K), the same was not possible for the scalar field. The smallest scale of the scalar field is referred to as the Bachelor length scale (η_B) and is a factor of $\sqrt{Sc} \approx 30$ smaller than η_K in the aforementioned studies. Therefore, the simulated diffusion process was affected by the numerical diffusion determined by the grid resolution.[61] For instance at $Re = 12000$, t_{mix} computed with 168×10^6 grid cells was ca. 13% higher than t_{mix} computed with 6×10^6 grid cells. Taking this into account, the latter one was regarded as a good compromise between computational resources and accuracy.[61] For the fluids with no density and viscosity difference, t_{mix} was found equal to about $48, 40$ and 35 for the three Re considered, decreasing with increasing Re.[56] This trend neither corresponds to the expected one in the turbulent regime, where $t_{mix} = const.$, nor the one in the transitional regime, where t_{mix} should scale with Re^{-1} according to Grenville,[40] but it is somewhat between the two.

D. Objectives of the present study

In the present study, we use the DNS method to investigate the flow and scalar fields inside an unbaffled tank agitated by a four-bladed radial impeller. The aforementioned two types of impeller blades, with regular and irregular (one-iteration fractal-like) blades, are considered in this study. Simulations are performed at $Re = 320$ and 1600, and $Sc = 1$.

In order to assess the mixing efficiency of the irregular with respect to the regular impeller, the mixing times are compared. To this end, we inject a passive scalar in the flow field and compute its evolution. The mixing performance is assessed using the time required to homogenize the distribution of the passive scalar. Moreover, we analyse the factors affecting the mixing time and leading to differences when regular and fractal impellers are compared. In addition to that, we assess the effect of Re while staying in the transitional regime.

It should be noted that stirred tanks are predominantly employed in industrial appli-

cations for liquid systems at $Sc \geq O(10^3)$.[24] Therefore, the study of mixing at $Sc = 1$ is not directly representative of industrial applications. The selection of $Sc = 1$ is mainly due to the computational limitations, since a higher Sc would decrease the size of the characteristic scales of the passive scalar fluctuations, require a finer resolution and an excessive computational power for the present DNS study. Nevertheless, the results obtained at $Sc = 1$ will serve as the first step of the performance comparison between the regular and irregular impellers, before the more practical and challenging cases are investigated. However, in the passive scalar situation considered here, the Schmidt number can be replaced by its heat diffusion analogue, the Prandtl number Pr, and our simulations could then correspond to potentially realistic laboratory experiments given that the Prandtl number of many common gases and even of water at normal temperatures is of order 1, e.g. $Pr \approx 0.7$ for air and ≈ 6.6 for water at room temperature.

The remainder of this paper is organized as follows: In the following section, we illustrate the flow configuration and describe briefly the numerical methodology employed. The scalar transport equation is then introduced, the details of the scalar injection and the methods used for the assessment of the scalar field are described. DNS results of the mixing time with regular and irregular blades are presented. Following that, the impact of the impeller type and Re on the mixing time is discussed. A simple mathematical model is suggested which is able to approximate the decay rate of the passive scalar fluctuations integrated over the tank volume. Finally, we close the paper with a summary and main conclusions.

II. Flow configurations and numerical methodology

The stirred tank investigated in the present work has a cylindrical geometry of equal height and diameter. A four-bladed impeller is located at mid-height. Figures 1a and 1b illustrate vertical and horizontal views of the impeller and the tank. The blade height and blade thickness are 1/10 and 1/100 of the tank diameter, respectively. Two types of impeller blades used in this study are shown in Figure 1c. These are referred to as regular and irregular (or fractal-like) blades and have equal frontal area. The same blades were

also used in our previous DNS study[2] and in the experimental study of Steiros et al.[1]

The radius of the irregular impeller is not uniform, as seen in Figure 1c. With R being the constant radius of the regular impeller, the furthest tip of the irregular blade is located at $r/R = 1.1$. The dimensions of the regular impeller are used for normalization purposes throughout the paper.

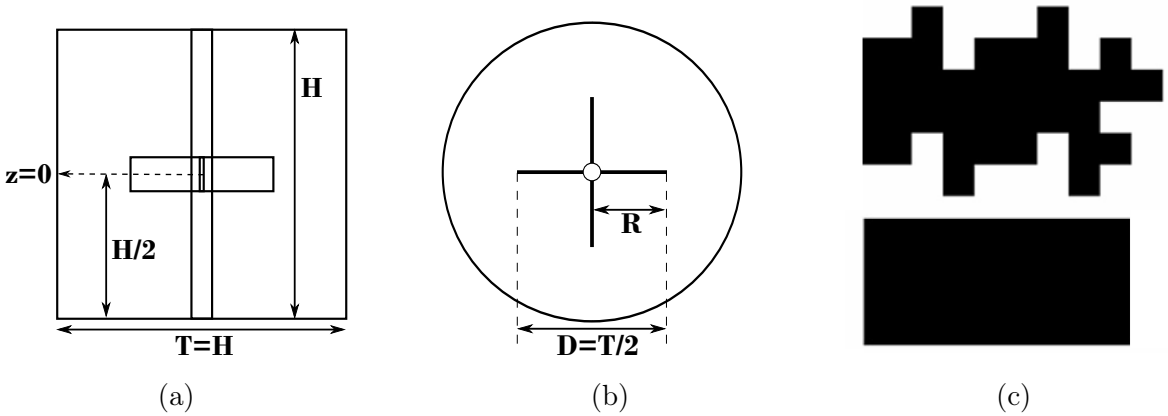

(a) (b) (c)

FIG. 1. Tank geometry, dimensions and blade shapes. a) Vertical view along the axis, b) horizontal view at the mid-height, c) irregular (one-iteration fractal-like) (top) and regular (bottom) blades.

DNS results presented in the paper were obtained with the incompressible in-house code "Pantarhei" based on the finite-volume method. This code was previously employed for LES of the flow in a baffled stirred vessel,[50,62] and for DNS studies of the flow around an airfoil,[63] the flow past a single square grid-element,[64] the flow in an unbaffled stirred vessel.[2] More details about the numerical methodology can be found in the last reference.

The Navier-Stokes equations were solved in a rotating reference frame, fixed to the impeller. Consequently, the momentum equations take the following form:

$$\frac{\partial \rho \vec{v}}{\partial t} + \nabla \cdot (\rho \vec{v} \otimes \vec{v}) = -\nabla p + \nabla \cdot \boldsymbol{\tau} - \rho[\, \vec{\omega} \times (\vec{\omega} \times \vec{x}) + 2\vec{\omega} \times \vec{v}\,], \tag{1}$$

where $\vec{v}$ denotes the instantaneous velocity vector in the rotating frame, $\boldsymbol{\tau}$ the viscous stress tensor and $\vec{\omega}$ the angular velocity of the frame. The origin of the coordinate system is at the mid-height of the tank, on the impeller axis. The position vector with respect to the origin is indicated by $\vec{x}$. Vector $\vec{\omega}$ points in the axial direction and its magnitude

is equal to $\Omega = 2\pi N$. The last two terms of Equation 1 stand for the centrifugal and Coriolis accelerations, respectively, and were treated as source terms. All solid surfaces have a no-slip condition. A moving wall boundary condition was imposed on the tank walls (i.e. top, bottom and side walls) to represent the relative motion with respect to the impeller. A prescribed velocity was imposed on these external walls equal to Ωr_w, where r_w is the radial distance of a wall point to the axis of rotation. The tank is closed at the top (solid wall), therefore free-surface depression was not considered.

The mixing inside the stirred tank was investigated at $Re = 320$ and 1600. For $Re = 320$, the computational domain was discretized using 13×10^6 and 21×10^6 grid cells for the regular and irregular impellers, respectively. For $Re = 1600$, these numbers were increased to 60×10^6 and 70×10^6, respectively. The details about the grid resolution and convergence study were presented by Başbuğ et al.[2] along with the validation of the code.

III. Scalar transport equation and injection details

The convection-diffusion equation for the evolution of a passive scalar in incompressible form reads:

$$\frac{\partial c}{\partial t} + v_i \frac{\partial c}{\partial x_i} = \Gamma \frac{\partial}{\partial x_i} \left(\frac{\partial c}{\partial x_i} \right) , \tag{2}$$

where the passive scalar is denoted by c and the diffusion coefficient by Γ. The equation has the same form for both inertial and rotational reference frames. Using the length scale D (the impeller diameter), the velocity scale ND and the time scale $1/N$ (i.e. the period of one impeller revolution), Equation 2 can be nondimensionalized and takes the following form:

$$\frac{\partial c}{\partial t^*} + v_i^* \frac{\partial c}{\partial x_i^*} = \frac{1}{Pe} \frac{\partial}{\partial x_i^*} \left(\frac{\partial c}{\partial x_i^*} \right) , \tag{3}$$

where $v_i^* = v_i/ND$, $t^* = t\,N$, $x_i^* = x_i/D$, $Pe = Re \times Sc$. For all simulations, Sc was taken equal to 1, hence the smallest scales of the flow and scalar fields are equal. Equation 2 was discretized using the finite volume method (FVM) and solved after the flow field was computed at every time step. A second-order central differencing scheme was used for

spatial discretization and an implicit second-order Euler method for time-marching. A zero normal-gradient boundary condition was imposed at the walls for the scalar field.

After the flow field has fully developed and the impeller power has converged to a constant value, the passive scalar was injected on the suction side of only one of the impeller blades using a constant flux boundary condition. The injection period was equal to a quarter of an impeller revolution for all simulations. Since the regular and irregular blades have the same frontal area, the total amount of scalar injected was the same. This method of injection does not introduce any momentum to the flow field and allows for the total amount of scalar to be precisely controlled.

The suction side of the blade was selected for the injection because the strong radial jet along this side of the blade advects the scalar away from the source and the up-and-down swinging motion of the radial jet[2] can redistribute the passive scalar in the axial direction. Moreover, the wake of the blade is the region with the highest velocity fluctuations. This region includes the trailing vortices which may be utilized to accelerate mixing. It was already emphasized in previous studies[65–67] that mixing is enhanced when the injection is located in the region with strongest instabilities.

In order to estimate the simulation time and memory requirements for computing the mixing time and to evaluate the computational quality of the solution, the homogenization of an injected passive scalar was simulated once for both impeller types at $Re = 320$ and 1600. These initial computations are referred to as "pilot runs", used only for the aforementioned tests and not for the conclusions regarding the mixing time.

The homogenization in a stirred vessel is a random process and is affected by the instantaneous flow field present at the time of injection. In order to take this influence into account for the mixing time evaluation, five different scalars are injected with a time lag equal to two impeller revolutions between the starting points of two consecutive injections. Although all five scalars were present in the same flow field instantaneously, they were solved separately and did not interact.

IV. Evaluation of scalar field

The volume averaged passive scalar is calculated as:

$$\bar{c} = \frac{\int c \, dV}{V_{tot}} \,, \tag{4}$$

where V_{tot} denotes the total volume of the vessel. Note that c is a function of space and time, $c = c(x_i, t)$, whereas $\bar{c}$ is a function of time only during the injection (after the end of injection it becomes constant). In all simulations, the final value of $\bar{c}$ was equal to $\bar{c}_\infty = 0.04$ after injection stopped. We checked that $\bar{c}$ increases linearly during the injection period and remains precisely constant afterwards for both impeller types and both Reynolds numbers.

The scalar can be decomposed into its volume average, $\bar{c}$ (that is also the long time limit value at every point after complete mixing), and the fluctuations around $\bar{c}$ as follows: $c = \bar{c} + c'$. The degree of mixing can be evaluated using the coefficient of variation (CoV) that is defined as the standard deviation of concentration measurements divided by the mean concentration.[24] This parameter was also referred to as coefficient of mixing,[51] or intensity of segregation.[31] It was commonly evaluated using a number of monitoring points or measurement locations.[24,31,51] In the present study, the main objective is to compare the mixing performance of the regular and irregular impellers as objectively and comprehensively as possible without reference to particular locations in the flow. Therefore, the CoV is computed using the information in the entire tank as follows:

$$CoV = \frac{1}{\bar{c}} \sqrt{\frac{\int (c')^2 \, dV}{V_{tot}}} \,, \tag{5}$$

When the value of CoV drops down to 5%, the scalar can be considered well mixed in a typical industrial application.[24] This degree of mixing means that the standard deviation of the spatial distribution is equal to 5% of the mean value. In the present study, the nondimentional time required to reach this degree of mixing will be referred to as t_{mix}. This value will be employed to make a comparison between different cases.

In order to assess the quality of the numerical resolution, we utilize the conservation equation of scalar variance, $(c')^2$. When Equation 3 is multiplied with c', and averaged over the volume, and assuming that the passive scalar injection has already stopped, we reach the following equation:

$$-\frac{1}{2}\frac{d}{dt^*}(\overline{c'^{\,2}}) = \frac{1}{Pe}\,\overline{\frac{\partial c'}{\partial x_i^*}\frac{\partial c'}{\partial x_i^*}}\,, \tag{6}$$

where the overbar denotes the volume averaging operation. The right-hand side of this equation denotes the dissipation rate of the scalar variance averaged over the entire tank, and quantifies the rate of homogenization dictated by scalar gradients. This term is computed at every time step on-the-fly, along with the value of $\overline{c'^{\,2}}$. The left-hand side of Equation 6 is computed in the post-processing stage, using a second-order central differencing scheme for the time derivative. If the resolution is not fine enough to resolve the smallest scales of the scalar field, there will be an imbalance in Equation 6 with the left-hand side taking a larger value than the right-hand side due to the numerical dissipation.

The discrepancy between the two sides of Equation 6 is computed for both impeller types and Re. This discrepancy is ca. 1% at $Re = 320$ and ca. 4% at $Re = 1600$ (in average over time). Both sides of Equation 6 are plotted against t^* in Figure 2 for the pilot run with the irregular impeller at $Re = 1600$. Since these terms decay exponentially, a discrepancy of 4% does not lead to a discernible difference in terms of their time evolution. Similarly, an error of 4% in CoV will not affect the prediction of t_{mix}. This result confirms that the employed computational grid is fine enough to resolve the small scales responsible for the scalar dissipation.

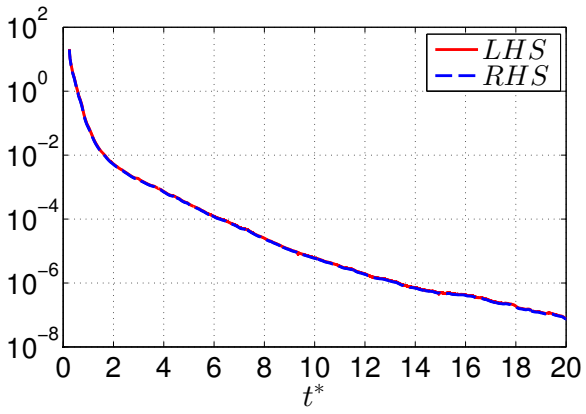

FIG. 2. The two sides of Equation 6 for the irregular impeller at $Re = 1600$.

V. Mixing times

In the present study, the mixing time (t_{mix}) is defined as the time that the homogenization process takes until CoV drops to 5%. Figures 3a-d demonstrate the CoV-curves of the five injections, for both impellers at $Re = 320$ and 1600. Although the five passive scalars are injected with a time lag of two impeller revolutions, the time is reset to $t^* = 0$ at the beginning of each injection for clarity of comparison.

When CoV is determined using a limited number of probe or measurement points, the homogenization curves exhibit strong oscillations[40,51] due to the fluctuations at the probe points. In the present cases, all curves in Figure 3 are smooth and monotonically decreasing. This is a consequence of the volume integration over the entire tank whereby locally extreme values are averaged out.

Figures 3a-d demonstrate that the mixing time of the five injections is spread between ca. 14.5 and 20.5 revolutions for the regular impeller, and between ca. 13.5 and 18 revolutions for the irregular impeller, taking results of both Re into account. The mixing time cannot be precisely predicted and varies between different realisations depending on the instant of the injection. Moreover, the findings suggest that the spread of mixing times is relatively narrower for the irregular compared to the regular impeller. The difference between the maximum and minimum t_{mix} is ca. 6 revolutions for the regular and 4.5 for the irregular impeller. This result indicates an improvement in the predictability of t_{mix} when the irregular impeller is used.

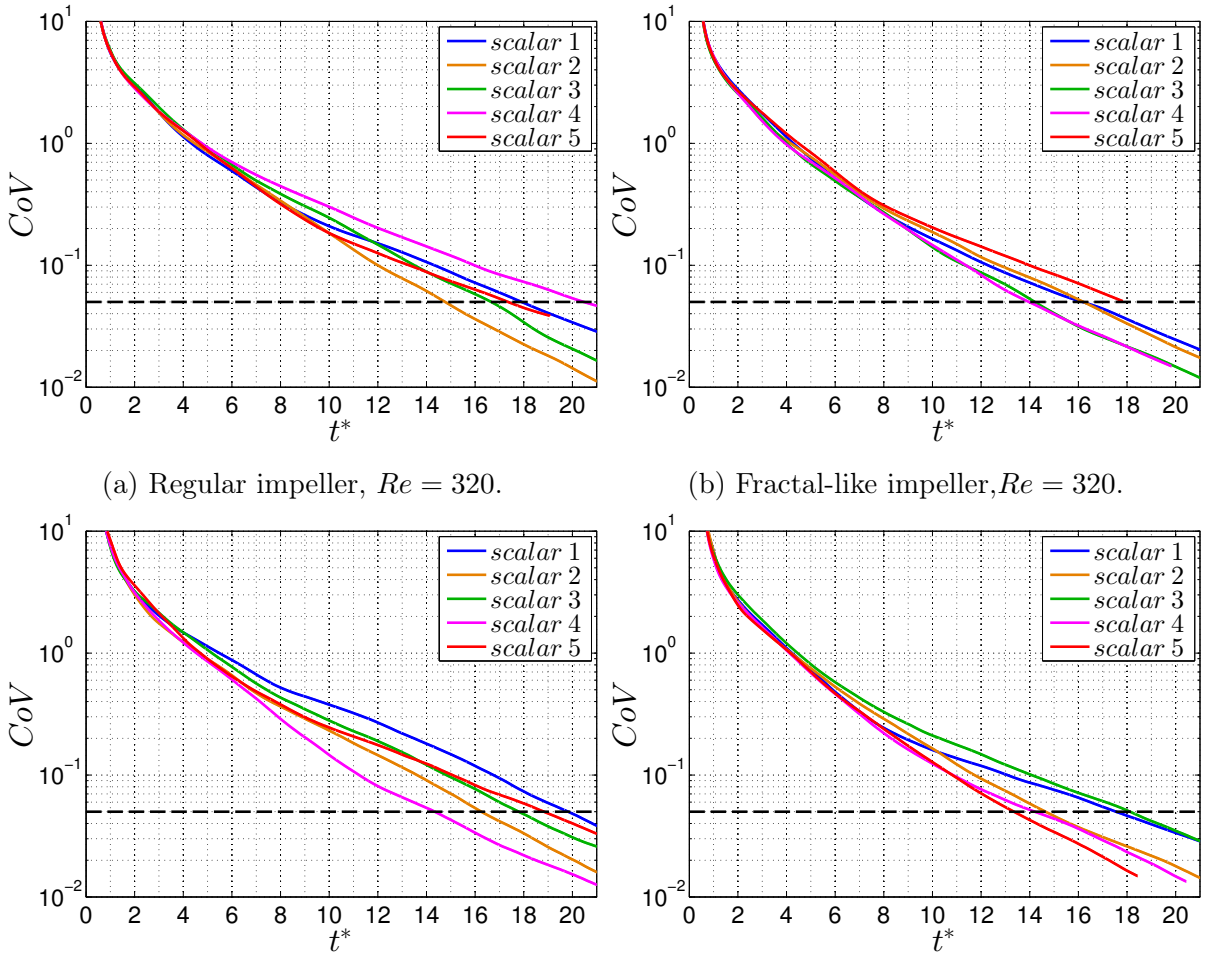

(a) Regular impeller, $Re = 320$.

(b) Fractal-like impeller,$Re = 320$.

(c) Regular impeller, $Re = 1600$.

(d) Fractal-like impeller, $Re = 1600$.

FIG. 3. Variation of CoV for five scalars shown for regular and irregular (fractal-like) impellers at both Re. The dashed horizontal line indicates $CoV = 5\%$.

In order to compare the mixing performance of the two impellers, the CoV-curves of the five realizations are averaged and the resulting curves are displayed in Figure 4. The average values of t_{mix} are presented in Table I along with the percentage difference between the two impeller types. The effect of impeller design is evident. The irregular impeller results in a shorter mixing time, by 10.3% at $Re = 320$ and by 12.0% at $Re = 1600$. We have added error bars in Figure 4, which make our results more transparent. The figure indicates that until the 8^{th} revolution, there is a clear improvement in CoV, given that the error bars do not overlap. After the 8^{th} revolution, there is increasing overlap, but the average is lower for the irregular blades. This result is confirmed for both Reynolds numbers.

To evaluate the mixing performance objectively, these findings must be combined

with the power consumption. At $Re = 320$, both impeller types draw equal power[2] (with $\langle N_p \rangle = 2.32$). Therefore, any decrease in the estimated t_{mix} for the irregular impeller is equivalent to an improvement in the mixing performance. At $Re = 1600$, $\langle N_p \rangle$ decreases from 1.59 to 1.47 when the regular blades are replaced by irregular ones, leading to a power reduction of ca. 8%.[2] Since the total energy consumption required to mix is proportional to $t_{mix} \times \langle N_p \rangle$ (for a fixed N), this value is estimated to be ca. 20% lower for the irregular impeller with respect to the regular one. This promising improvement provides motivation for further investigation of the performance of irregular, fractal-like, impellers in other mixing applications in future research.

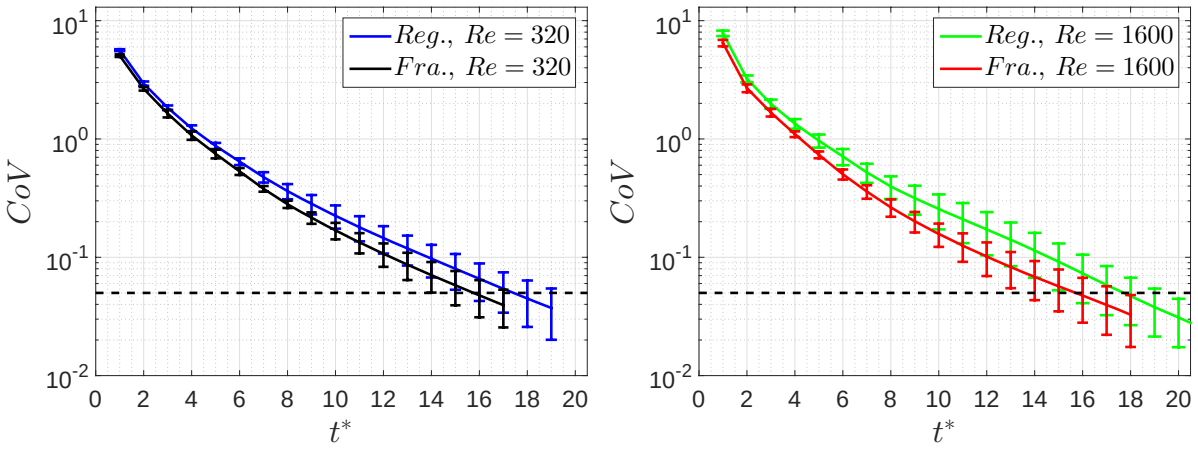

(a) $Re = 320$. (b) $Re = 1600$.

FIG. 4. Average CoV curves for the two Re numbers examined. The black dashed line indicates $CoV = 5\%$. Reg. stands for the regular and Fra. for the fractal-like (irregular) impeller. Vertical lines are error bars (± one standard deviation from the mean).

TABLE I. Average mixing time t_{mix}. The difference between the regular and fractal-like/irregular impellers is presented in the rightmost column.

	Regular	Fractal-like	Difference
$Re = 320$	17.4	15.7	10.3%
$Re = 1600$	17.7	15.7	12.0%

It can be argued that five realisations of passive scalar homogenization may not be sufficient to obtain a firm conclusion about t_{mix} considering the spread of data, as seen in Figure 3. However, the influence of the impeller design on the trend of the averaged CoV-curves is very similar at both Re, as shown in 4. This decrease of t_{mix} at both Re,

when the regular blades are replaced by irregular ones, improves the reliability of the findings.

The results show that the increase in the Re from 320 to 1600 does not significantly affect the trend of CoV-curves or t_{mix}. This seems counter-intuitive considering that the range of Re examined is in the transitional regime. Indeed, the results showed that the power number decreases significantly when Re is increased from 320 to 1600, e.g. from 2.32 to 1.59 for the regular impeller. As mentioned earlier, Grenville[40] suggested for the transitional regime the following relation: $t_{mix} = 183^2 \ \langle N_p \rangle^{-2/3} \, Re^{-1} (T/D)^2$. With $Re = 320$ and $\langle N_p \rangle = 2.32$, this relation gives $t_{mix} = 240$. With $Re = 1600$ and $\langle N_p \rangle = 1.59$, it results in $t_{mix} = 61$, considering the parameters of the regular impeller. Clearly, the values of t_{mix} given by Grenville's relation are much higher than our numerical predictions. Moreover, this relation predicts a decrease in t_{mix} with increasing Re. These two major differences between the estimates obtained with Grenville's relation and the simulations can stem from the large difference in Pe which determines the influence of the diffusion term in the scalar transport equation (see Equation 3). Pe was $O(10^7)$ in experiments of Grenville[40] whereas it was $O(10^2)$ - $O(10^3)$ in our simulations. This influence will be discussed later in detail.

In the next section, we identify the characteristics of the flow and scalar fields that determine the mixing process, and try to provide a physical explanation for the observed mixing time results.

VI. Analysis of mixing times

A. Evolution of the iso-scalar surfaces

In order to shed more light on the mixing times for regular and irregular impellers, we investigate the evolution of iso-scalar surfaces. These surfaces are by definition normal to the scalar gradient driving the diffusive mixing. The fluid advection can stretch or fold the isosurfaces, hence increase the area for the diffusive flux to operate.[68] We use the iso-scalar surfaces $c = \bar{c}$, since such iso-surfaces exist throughout the entire process until full

homogenization. We can imagine that the flow domain is divided into two subdomains: one where c is higher than the equilibrium value (i.e. $c > \bar{c}$) and another where c is lower (i.e. $c < \bar{c}$). The diffusion process can transport c from one to the other subdomain only through the iso-scalar surface $c = \bar{c}$. Therefore, the investigation of this surface can be used for the interpretation of the mixing process, and in the explanation of the different mixing times observed between different injections and impeller types. We start this analysis with an illustration of the scalar field using contours and iso-scalar surfaces.

Figure 5a illustrates iso-contours of $c/\bar{c}$ at the mid-height plane of the tank with the regular impeller at $Re = 1600$, half a revolution after the start of injection. The passive scalar, injected on the suction side of the blade, is clearly carried along the path of the trailing vortices. The iso-scalar surface $c = \bar{c}$ at the same instant is shown in Figure 5b. Although the scalar is still profoundly segregated at this stage, the isosurfaces indicate the patterns of stretching and folding by the flow field before the scalar is dispersed in the whole tank.

The scalar field two revolutions after the start of injection is illustrated in Figure 6. The contour plot of $c/\bar{c}$ on the vertical plane 30° behind a blade is shown in Figure 6a. It indicates that the strong radial jets have already transported the passive scalar towards the side walls of the tank. Smaller scales are also emerging in the scalar field, as demonstrated in Figure 6b that displays the iso-scalar surface. This has led to a significant increase in the area of isosurfaces, which can be noted when Figures 5b and 6b are compared.

The growth of the aforementioned surface area over the entire computational time is illustrated in Figure 7 for all cases. The curves corresponding to different injections start from their actual injection times, i.e. $t^* = 0, 2, 4, 6, 8$, so that their behaviour can be compared because the same instantaneous flow field is advecting all five scalars simultaneously. For normalization purposes, the total area of the outer wall surfaces is used (top, bottom and side walls), which is $A_W = 1.5\,\pi\,T^2$ (T is the tank diameter equal here to tank height, see Figure 1). The five curves, corresponding to the five injections, are averaged and illustrated in Figure 8, in order to highlight the effect of the impeller

type and Re.

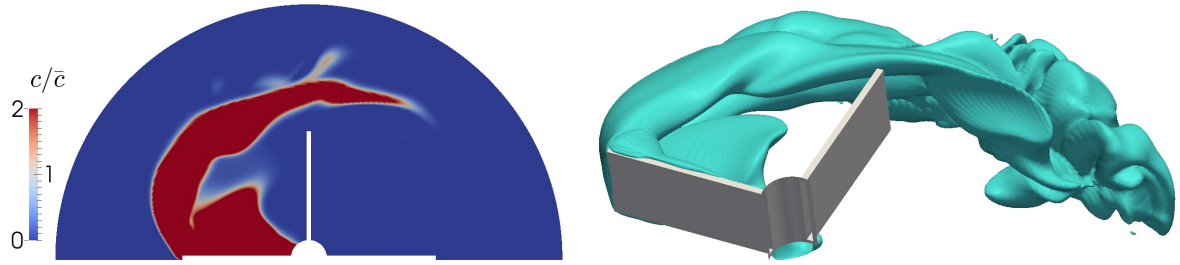

(a) (b)

FIG. 5. (a) Contour plot of $c/\bar{c}$ at the mid-height plane. (b) The iso-scalar surface $c = \bar{c}$. Regular impeller at $Re = 1600$, half a revolution after the start of injection.

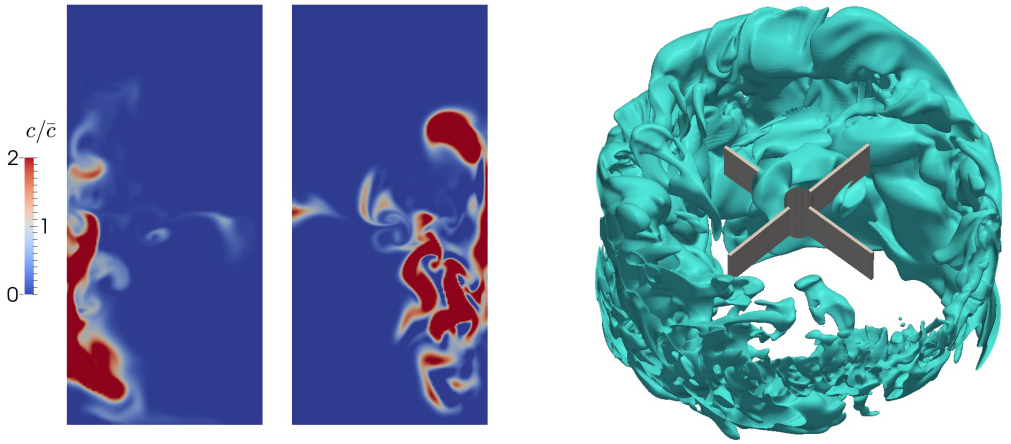

(a) (b)

FIG. 6. (a) Contour plot of $c/\bar{c}$ on the vertical plane 30° behind a blade (the cross-section of the shaft is left vertically blank at the centre of the plot). (b) The iso-scalar surface $c = \bar{c}$. Regular impeller at $Re = 1600$, two revolutions after the start of injection.

As seen in Figure 7, the iso-scalar surfaces grow continuously during the initial two revolutions after the injection. Figure 8 shows that on average A/A_W is equal to 0.6 for $Re = 320$, and to 1.3 for $Re = 1600$, at the end of the first two revolutions regardless of the impeller type. Moreover, the curves of every realization collapse very well during the aforementioned period for $Re = 320$, and for $Re = 1600$ they start to deviate after ca. 1.5 revolutions (this can be seen more clearly when all curves in Figure 7 are plotted together starting from $t^* = 0$; the figure is not shown here). In other words, the initial

growth rate of the iso-scalar surfaces (i.e. the slope of curves in Figure 7) is equal for every realization, and only different at different Re. This can be explained as follows: The segregated state of the passive scalar seen in Figure 5 becomes dispersed as shown in Figure 6 and the length scales of the flow field determine the level of dispersion (i.e. the scale of segregation), hence the area of iso-scalar surfaces. Since the length scales of the flow field become smaller at higher Re, the initial growth rate of A/A_W gets steeper, which is also evident in Figure 8.

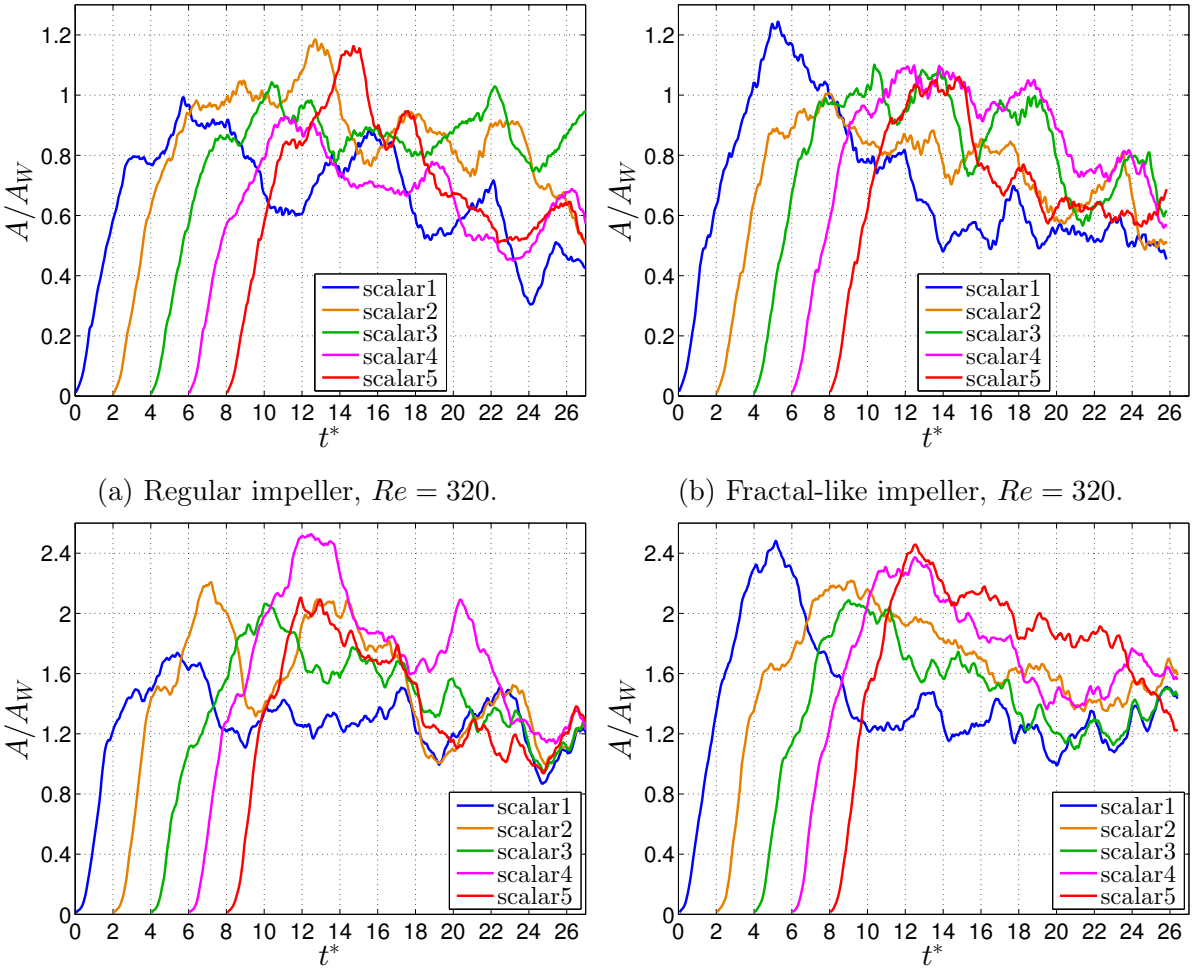

(a) Regular impeller, $Re = 320$.

(b) Fractal-like impeller, $Re = 320$.

(c) Regular impeller, $Re = 1600$.

(d) Fractal-like impeller, $Re = 1600$.

FIG. 7. Normalized area of iso-scalar su rfaces for five realizations in all cases.

This dispersion, and the consequent rapid stretching, is also the reason of the steep decrease of the CoV values during the initial period (see Figure 3). Similarly, the curve of $-\frac{1}{2}\frac{d}{dt}(\overline{c'^2})$ (see Figure 2) exhibits a sharp drop for the first two revolutions, that is followed by a milder slope for the remainder of the process.

After the initial dispersion, the passive scalar starts to circulate inside the tank along with the flow. At the same time, the areas of iso-scalar surfaces exhibit strong fluctuations as seen in Figure 7. We can distinguish some fast fluctuations with a small amplitude and several peaks per revolution, which are easily recognized over the periods when A/A_W does not exhibit a steep change. This can be noted for instance in Figure 7a on the curve of the scalar-1 at $t^* = 6 - 8$, $t^* = 10 - 12$, or $t^* = 18 - 20$. These oscillations in A/A_W possibly stem from the instabilities of the trailing vortices and the radial jet observed at the frequency $f' \approx 3$ and discussed in our previous paper.[2] In addition to the fast fluctuations in A/A_W, the curves in Figure 7 exhibit larger peaks which appear irregularly and over large time scales such as several revolutions. It is noted that these can appear in curves of several different scalars simultaneously. For instance in Figure 7a, the curves of scalar-1 and scalar-3 exhibit the same trend from $t^* = 20$ to 24, although they are injected with a time difference equal to four revolutions; this can also be noted in Figure 7c between the curves of scalar-1 and scalar-2 from $t^* = 18$ to 26 where both curves simultaneously exhibit a long wave. This phenomenon can be related to the slow instabilities already reported[2] that appear at $f' \approx 0.12$ in the power spectral density (PSD) of the axial velocity component.

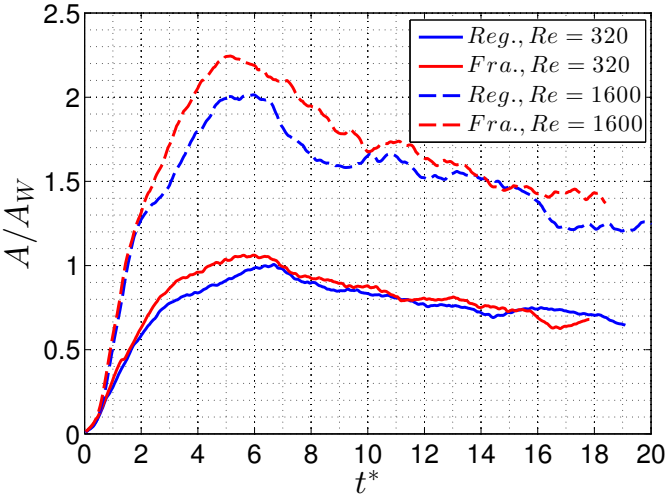

FIG. 8. Area of isosurfaces averaged for the five injection in all cases.

Focusing on Figure 8 and comparing the results of averaged curves, several interesting features can be detected. It is seen that the fractal-like/irregular impeller leads to a

larger area of iso-scalar surfaces on average than the regular impeller, at both Re. This can explain the lower t_{mix} predicted for the fractal-like/irregular impeller. The correlation between A/A_W and t_{mix} is assessed at the end of this and in the next subsections.

Moreover, it is observed that the area of iso-scalar surfaces are ca. twice as large at $Re = 1600$ than at $Re = 320$. This is a consequence of the changes in the velocity field as Re is increased. Also the scalar gradients are expected to be steeper at $Re = 1600$, since the iso-scalar surfaces are more stretched. One can expect that these characteristics enhance mixing and result in a lower t_{mix}. However, the increase in Re has another impact that must be taken into account. There is a factor $1/(Re\,Sc)$ in front of the diffusion term of Equation 3 (the increase in Re is realized in simulations by setting a lower ν, and is accompanied by a proportional decrease in Γ, since Sc is kept constant). Therefore, the increase in Re weakens the diffusion term, which counteracts the mixing enhancement due to larger isosurfaces. Although the increase in Re from 320 to 1600 creates larger isosurfaces and steeper gradients, this does not decrease t_{mix}, because the molecular diffusion is weaker at $Re = 1600$.

In Grenville's experiments,[40] where Pe is very high (e.g. $O(10^7)$), the diffusion term is very small compared to the advection term. We already know that in the fully turbulent regime, where Pe is very high and flow field is fully developed, any increase in Re, hence Pe, does not affect t_{mix}.[24,32] Taking these into account, when Re is increased in the transitional regime, the changes in the diffusive term can be insignificant (due to high Pe) compared to the drastic development of the velocity field and the increase in the area of isosurfaces. Therefore, the aforementioned author might have observed $t_{mix} \backsim Re^{-1}$ in the transitional regime due to the increasing area of isosurfaces. Comparing Grenville's results with ours, we can infer that the Re-scaling of t_{mix} in the transitional regime can be strongly affected by Pe.

In what follows, we try to relate the area of iso-scalar surfaces $c = \bar{c}$ with the rate of homogenization. First, we conduct a qualitative evaluation and compare the area of iso-scalar surfaces of the five injections in one case, e.g. for the regular impeller at $Re = 1600$. To this end, Figure 9 illustrates the running averages of the aforementioned isosurfaces.

When this is considered together with Figure 3c showing the CoV-curves of the same case, it is observed that the scalar injections with the higher value of averaged A/A_W also present faster mixing. Moreover, the trends of the CoV-curves in Figure 3c seem to be related with the trends of A/A_W of the corresponding scalars. For instance, scalar-5 (red curve) which has a lower CoV than scalar-3 (green curve) until $t^* = 12$, has also a larger averaged A/A_W. After $t^* = 12$, the averaged A/A_W of scalar-5 drops below the curve representing scalar-3. Eventually, scalar-3 presents a larger average A/A_W and exhibits a faster mixing than scalar-5. Next, we try to correlate the decrease of the CoV with the area of iso-scalar surfaces using a simple mathematical model.

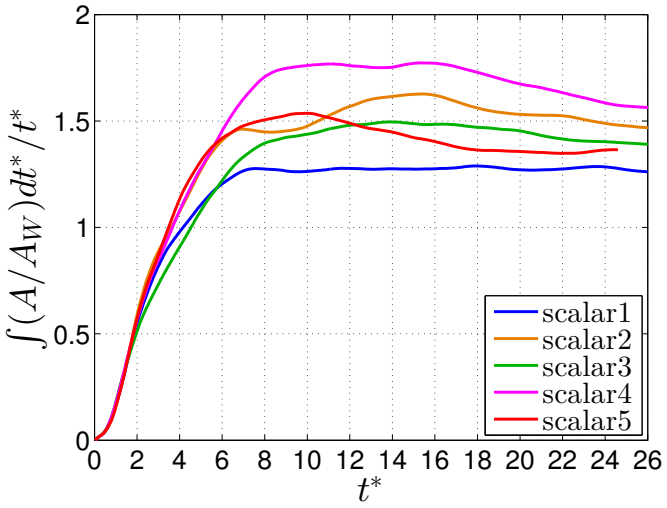

FIG. 9. Running average of the normalized area of isosurfaces for regular impeller at $Re = 1600$.

B. Decay rate scaling

As defined by Equation 5, CoV is proportional to the square root of $(\overline{c'^2})$. Moreover, Equation 6 shows that the negative time derivative of $(\overline{c'^2})$, i.e. the decay rate, depends crucially on the scalar gradients. We now assess if the volume integral of the decay rate can be characterized only by the scalar gradients in the vicinity of the iso-scalar surface $c = \bar{c}$. The gradient of c normal to the aforementioned surface can be approximated using a length scale characteristic of scalar diffusion, hereafter denoted by η, and the corresponding increment of c. We define η as the average distance between two iso-scalar

surfaces $c = c_1$ and $c = c_2$, where c_1 and c_2 deviate only a little from $\bar{c}$, i.e. $c_1 = \bar{c} + \Delta c$ and $c_2 = \bar{c} - \Delta c$ with a small enough Δc. Since $c_1 - c_2 = 2\Delta c$, the aforementioned gradient is approximated with $2\Delta c/\eta$. After nondimensionalization ($\eta^* = \eta/D$), this is substituted into Equation 6 which takes the following form:

$$-\frac{1}{2}\frac{d}{dt^*}(\overline{c'^2}) = \frac{1}{Pe}\overline{\frac{\partial c'}{\partial x_i^*}\frac{\partial c'}{\partial x_i^*}} \backsim \frac{1}{Pe}\left(\frac{2\Delta c}{\eta^*}\right)^2 . \tag{7}$$

The average diffusion length η is calculated as follows: $\eta = V_\Delta/A$, where A is the area of the iso-scalar surface $c = \bar{c}$, and V_Δ is the volume confined between the two iso-scalar surfaces, $c = c_1$ and $c = c_2$. The value selected for Δc needs to be very small compared to $\bar{c}$, since we focus on the gradients on the iso-scalar surface $c = \bar{c}$. On the other hand, the model should be independent of this choice. When the selected value (Δc) is increased, the volume V_Δ grows as well, hence the length scale $\eta = V_\Delta/A$ increases. Therefore, the ratio $2\Delta c/\eta$ is not expected to exhibit a strong dependence on Δc, provided Δc is small enough. In order to confirm this, the influence of Δc is tested below.

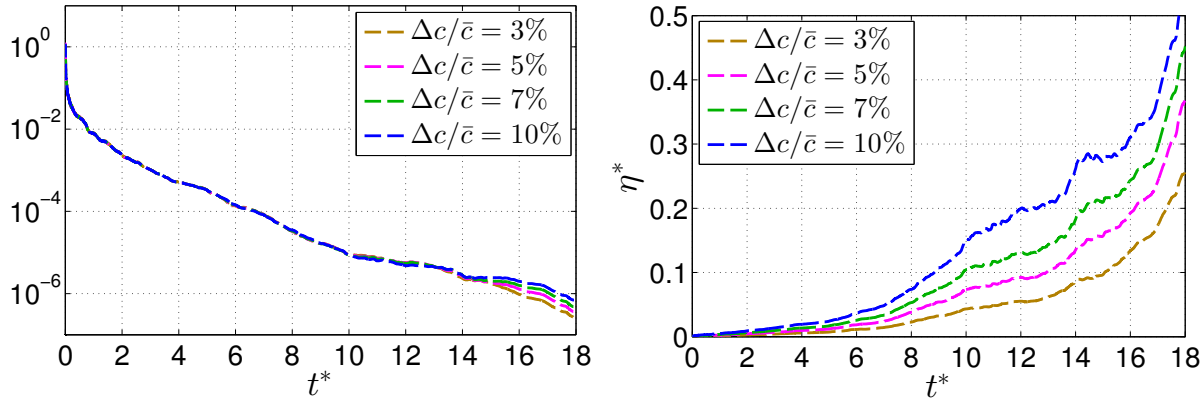

(a) (b)

FIG. 10. (a) The rightmost term in Equation 7 is computed using four different values of Δc. (b) The trend of η^* against t^*. For scalar-1 of the regular impeller at $Re = 320$.

This test is conducted using the data of scalar-1 of the regular impeller at $Re = 320$. The rightmost term in Equation 7 is computed using several different values for Δc and compared in Figure 10a. The four dashed lines with different colors are obtained with $\Delta c/\bar{c} = 3\%, 5\%, 7\%$ and 10%. Figure 10a illustrates that these curves do collapse until ca. $t^* = 15$. After $t^* = 15$, the four curves start to deviate which can be explained as follows.

Until ca. $t^* = 15$, the length scales η^* based on different values of Δc exhibit a very slow growth as shown in Figure 10b. After $t^* = 15$, the diffusive length scales grow quickly and at $t^* = 18$ the value of CoV has dropped to 0.05 which corresponds to the well-mixed state (see Figure 3a). These results suggest that in the last stage shortly before complete homogenization, the average distance between the isosurfaces $c_1 = \bar{c} + \Delta c$ and $c_2 = \bar{c} - \Delta c$ grows quickly and the scalar gradients normal to the iso-scalar surface $c = \bar{c}$ cannot be computed accurately using $2\Delta c/\eta$.

The test case discussed above has shown that the model does not exhibit a significant dependence on the selected value of Δc (for $\Delta c/\bar{c} < 10\%$, and for the regular impeller at $Re = 320$), until the last 3 revolutions before the well-mixed state. Therefore, we set $\Delta c/\bar{c} = 5\%$ for the rest of the discussion. When this value of Δc and $\eta = V_\Delta/A$ are plugged into the model, it takes the following form:

$$\frac{1}{Pe}\left(\frac{2\Delta c}{\eta^*}\right)^2 = \frac{(0.1\,\bar{c}\,D)^2}{Pe}\left(\frac{A}{V_\Delta}\right)^2 . \tag{8}$$

This is computed for all five realizations and the curves corresponding to the five realizations are averaged. Moreover, the five curves obtained with the exact calculation of the decay rate are averaged, as well. The model and the exact calculation are compared in Figure 11 for every case studied. The results show that the model is able to predict the trend of the decay rate correctly except for the first two revolutions. During the first two revolutions, the model underestimates the decay rate severely. It was already shown in Figures 5 and 6 that the passive scalar is significantly segregated during this period. There are very steep gradients inside the segregated regions, away from iso-scalar surfaces $c = \bar{c}$ which bound the segregated bulks. It is likely that the diffusion due to the internal gradients outweigh the gradients near the iso-scalar surface $c = \bar{c}$ in this initial phase.

If the curves generated with the model are scaled up with a constant factor and collapse with the curve of the decay rate, this would show that the decay rate scales with $(A/V_\Delta)^2$. To evaluate this scaling factor, we compute the ratio of the exact calculation of the decay

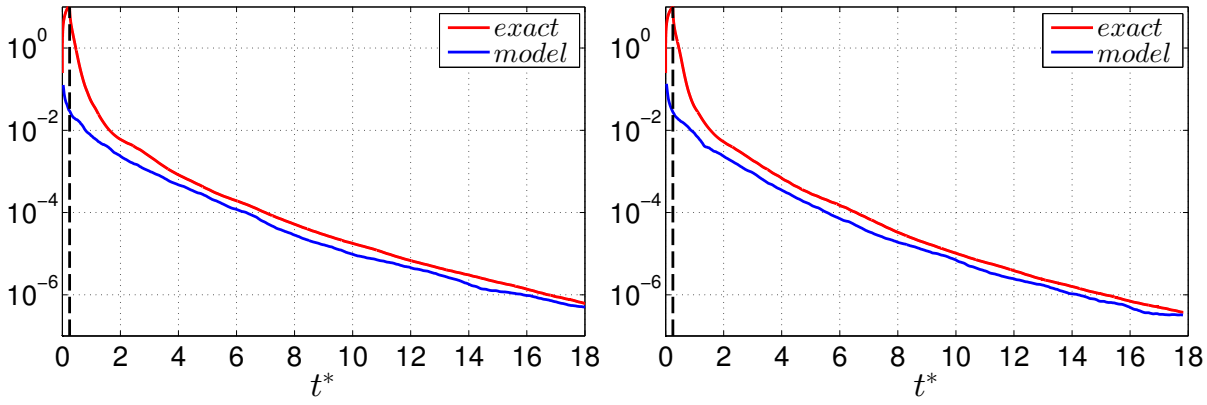

(a) Regular impeller, $Re = 320$.

(b) Fractal-like impeller, $Re = 320$.

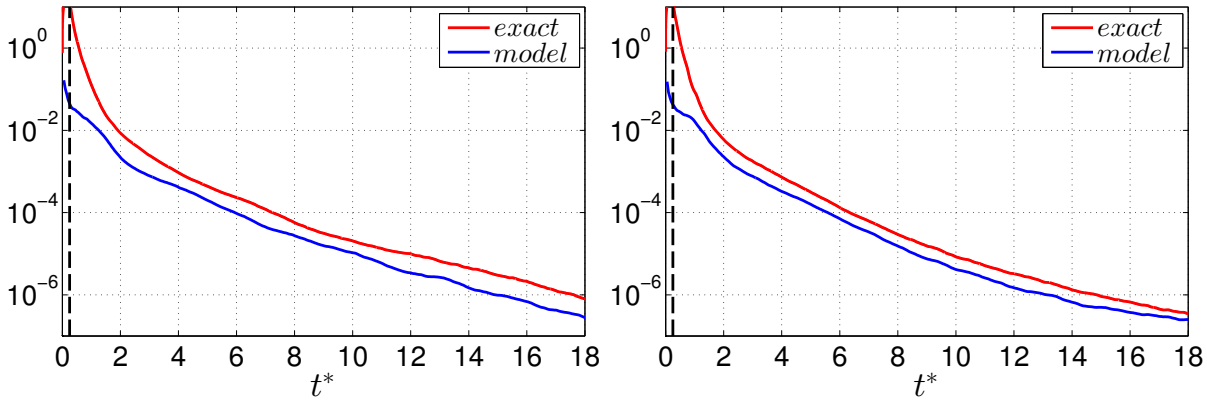

(c) Regular impeller, $Re = 1600$.

(d) Fractal-like impeller, $Re = 1600$.

FIG. 11. Exact calculation of the decay rate (exact) and the model based on $\Delta c/\bar{c} = 5\%$ (model) as expressed in Equation 8. The curves obtained with five realizations are averaged in all cases. The vertical dashed lines indicate the time when the injection stopped.

rate to the model as follows:

$$K = \overline{\frac{\partial c'}{\partial x_i^*}\frac{\partial c'}{\partial x_i^*}}\left(\frac{2\Delta c}{\eta^*}\right)^{-2} \tag{9}$$

This ratio, K, is plotted in Figure 12 against time. After ca. $t^* = 3$, the curves converge to the band between 1.5 and 2, except for the curve representing the regular impeller at $Re = 1600$, which fluctuates between 2 and 3. The fluctuations of K are probably the result of the low number of samples, since only five realizations are available. Although the nondimensional value of the decay rate changes over six orders of magnitudes (see Figure 11), the ratio K remains relatively constant after ca. $t^* = 3$. The model based on the area of the isosurfaces is therefore able to predict at least the order of magnitude of

the decay rate over a very broad range.

These findings suggest that for the scalar fields with larger iso-scalar surfaces, the mixing is enhanced. It was already shown in Figure 8 that the fractal-like/irregular impeller leads to a larger iso-scalar surface area on average, at both Re. We have suggested that this can be the reason of the shorter t_{mix} provided by the fractal-like/irregular impellers. The simple model developed in this section supports this conclusion.

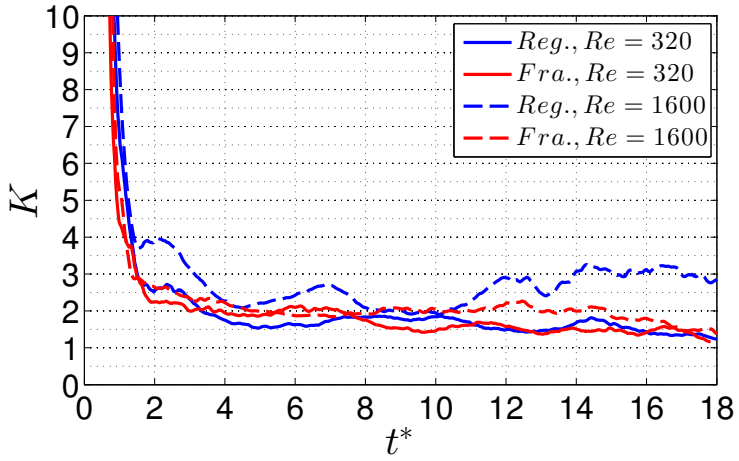

FIG. 12. The ratio K of the exact decay rate to the model value (equation 9), for both impellers and Re.

C. Spatial distribution of isosurfaces

In this subsection, we determine the regions inside the tank where the iso-scalar surfaces are frequently created, and understand the patterns they illustrate while they are stretched. From this we can infer which aspects of the flow field have the most dominant influence on the growth of isosurfaces.

In order to detect the location of the iso-scalar surfaces $c = \bar{c}$, a new variable $g(x_i, t)$ is defined as a function of space and time as follows: In any grid cell and time step, $g(x_i, t)$ is equal to 1 if the iso-scalar surface $c = \bar{c}$ is present in the cell at that instant, otherwise it is equal to 0. In practice, the isosurface $\bar{c}$ is detected in a cell if $c(x_i, t)$ is such that $0.99 < c/\bar{c} < 1.01$. Variable $g(x_i, t)$ is computed and averaged over a certain period of time. The time-averaged value is denoted by $\langle g(x_i) \rangle$, and it is a function of space only. Physically, it represents the fraction of time when the isosurface $c = \bar{c}$ is present at a given

location. The higher the value, the higher the probability of appearance of the isosurface $c = \bar{c}$.

The calculation and averaging started at $t^* = 2$, since the continuous growth of the isosurfaces during the first two revolutions was attributed to the dispersion of the initially segregated bulk of the passive scalar. Hence, this period exhibits different characteristics compared to the rest of the homogenization process and is excluded from the analysis presented in this subsection. The averaging is continued for the duration of 9 impeller revolutions, i.e. over the period $t^* = 2 - 11$. Therefore, the computation covers only the time until the length scale η^* starts growing rapidly (see Figure 10b). The calculation of $\langle g \rangle$ is performed for both impeller types, but only for scalar-1 at $Re = 320$. The result of this calculation gives the spatial distribution of $\langle g \rangle$ illustrated in Figure 13 on a vertical cut-plane 15° behind the blades.

As seen in Figure 13, the highest values of $\langle g \rangle$ appear along the radial jet, along the tank walls and the impeller shaft. It is noted that these patterns of $\langle g \rangle$ show similarity to the mean flow circulation inside the tank. For comparison, the mean flow field is illustrated in Figure 14 on the same plane 15° behind the blades. The contours in that figure display the magnitude of the projected and normalized mean velocity, i.e. $\sqrt{U_r^2 + U_z^2}/U_{tip}$, where U_r and U_z are the mean radial and axial velocity components, respectively, and U_{tip} denotes the blade tip velocity ($U_{tip} = \Omega R$). The arrows show the direction of the mean velocity vector projected on the plane. The comparison between contours in Figure 13 and the flow patterns in Figure 14 suggests that the iso-scalar surfaces are stretched along the mean flow circulation. Especially, the contours of $\langle g \rangle$ near the top and bottom walls of the tank show that the iso-scalar surfaces are curved along the trajectory of the mean flow. These findings indicate that the mean circulation has a significant impact on the stretching of the iso-scalar surfaces.

We avoid comparing Figures 13a and 13b in order to reach a conclusion about specific differences between the regular and fractal-like/irregular impellers, but use these only to evaluate the overall patterns. This is because these figures are obtained using only one injection (scalar-1).

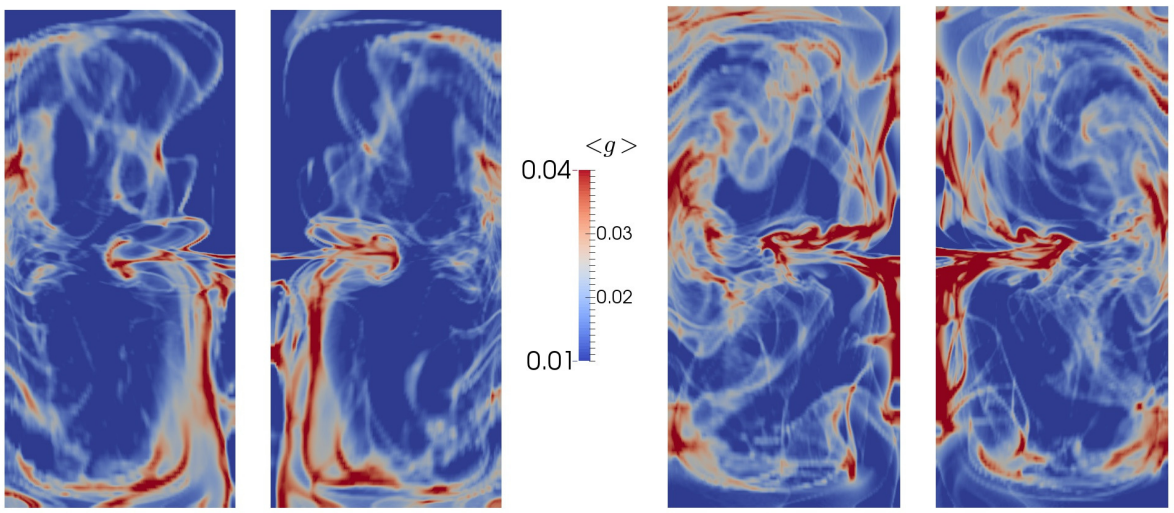

(a) Regular impeller. (b) Fractal-like impeller.

FIG. 13. Contours of $\langle g \rangle$ on a cut-plane 15° behind the blades, at $Re = 320$ (the cross-section of the shaft is left blank).

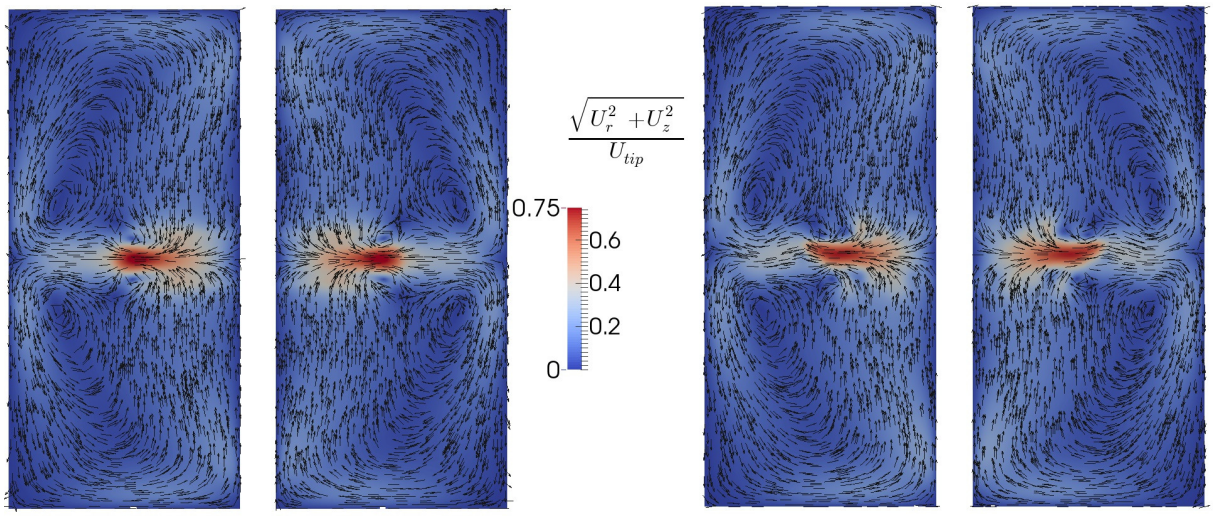

(a) Regular impeller. (b) Fractal-like impeller.

FIG. 14. The arrows show the direction of the mean velocity projected on the cut-plane (15° behind the blades), and the contours display its magnitude normalized with the blade tip speed, at $Re = 320$ for both impeller types (the cross-section of the shaft is left blank).

Taking into account that the main flow circulation plays an important role in the stretching of the iso-scalar surfaces, this effect can be augmented if the flow rate is increased. It was already shown in our previous paper[23] using a control volume around the impeller, that the fractal-like/irregular impeller results in a higher flow rate with respect to the regular impeller, by 7.3% at $Re = 320$ and by 10.3% at $Re = 1600$. This increase

in flow rate can be the major factor leading to a larger area of the iso-scalar surfaces for the fractal-like/irregular impeller at both Re, as shown in Figure 8. As a result of these factors, the homogenization of the injected passive scalar is accelerated when the fractal-like/irregular impeller is used instead of the regular impeller.

VII. Summary and Conclusions

Previous studies demonstrated a reduction in power consumption of an unbaffled stirred vessel when regular blades were replaced with fractal-like/irregular blades, by $11-12\%$ at $Re = 1-2\times10^5$ and by 8% at $Re = 1600$, whereas there was no difference at $Re = 320$.[1,2] In order to make a complete performance comparison, in the present work we have evaluated the mixing time required to homogenize an injected passive scalar with the regular and fractal-like/irregular impellers, by means of DNS at $Re = 320$ and 1600, where $Sc = 1$.

The nondimensional mixing time, t_{mix} is determined as the time when the value of CoV drops to 5%, where CoV is computed using the entire scalar field. In each case, i.e. for both impeller types and Re, five separate scalars are injected with a time lag equal to two impeller revolutions. In order to compare different cases, the CoV-curves of the five realizations are averaged and the average t_{mix} is determined. Based on these results, the irregular impeller leads to a shorter mixing time by 10.3% at $Re = 320$ and by 12.0% at $Re = 1600$. Since the total energy consumption required for the mixing process is proportional to $t_{mix} \times \langle N_p \rangle$ (for a fixed N), this is estimated to be 10.3% lower at $Re = 320$ and 20% lower at $Re = 1600$, for the irregular impeller with respect to the regular one. These findings motivate further studies of fractal-like and irregular impellers in other mixing applications.

When the performance of a certain impeller type at two different Re is compared, it is observed that Re does not affect t_{mix} significantly. This behaviour is expected at fully turbulent regime[24] whereas the considered Re values are in the transitional regime. In order to explain this result as well as the different mixing times obtained with the regular and irregular impellers, the evolution of the iso-scalar surfaces $c = \bar{c}$ is analysed. These

surfaces characterize the amount of contact area over which the molecular diffusion can act. The aforementioned surfaces are computed for the five realisations in each case. It is observed that these surfaces grow almost linearly during ca. the first two revolutions in every case, and the slope of this growth only depends on the Re. Afterwards, they stabilize around a certain level and fluctuate around that. These fluctuations can be linked to the large scale instabilities observed in the flow field discussed by our previous work.[2] When the time-averaged area of isosurfaces are compared among the five realizations obtained in the same case, it is determined that the realizations which result in a larger area, do also lead to a shorter t_{mix}. Moreover, when the isosurface areas of the five realizations are averaged and compared, it is noted that the irregular impeller generates larger iso-scalar surfaces on average with respect to the regular impeller at both Re. This can be the reason of the faster mixing presented by the irregular impeller.

Furthermore, the area of the isosurfaces grows ca. twice as large at $Re = 1600$ than at $Re = 320$. This stems from the changes in the velocity field as Re rises. On the other hand, the diffusive term of the scalar transport equation is scaled by $1/(ReSc)$, therefore the increase in Re weakens the diffusion. Our findings suggest that the decreasing strength of the molecular diffusion counteracts the effect of the increasing area of isosurfaces. Therefore, t_{mix} is not significantly affected by the increase in Re. However, this behaviour can be different for the cases with very high Pe, where diffusion is much weaker than advection.

In order to provide a quantitative correlation between the decay of CoV and the area of iso-scalar surfaces (A), a simple mathematical model is devised. This model approximates the integral decay rate using the scalar gradients in the vicinity of the iso-scalar surfaces $c = \bar{c}$. The results suggest that the decay rate of $\overline{c'^2}$ scales with A^2, and support the aforementioned conclusion that t_{mix} is linked to the area of the isosurfaces.

Finally, we determined the regions in the flow field where the aforementioned surfaces are predominantly created. It is noted that these surfaces are stretched along the mean flow circulation inside the vessel, i.e. along the radial jets, the tank walls and the impeller shaft. It has already been shown[23] that the fractal-like/irregular impellers generate a

higher flow rate with respect to the regular impeller, by 7.3% at $Re = 320$ and by 10.3% at $Re = 1600$. This difference in the flow rate can be the dominant factor leading to the larger average area of the iso-scalar surfaces in the tank with the fractal-like/irregular impeller.

Acknowledgements

The authors acknowledge the EU support through the FP7 Marie Curie MULTI-SOLVE project grant no. 317269, the computational resources allocated in ARCHER HPC through the UKTC funded by the EPSRC grant no. EP/L000261/1 as well as the CX2 facility of Imperial College London. JCV also acknowledges ERC Advanced Grant 320560.

Literature cited

[1] Steiros K, Bruce PJK, Buxton ORH, Vassilicos JC. Power consumption and form drag of regular and fractal-shaped turbines in a stirred tank. *AIChE Journal*. 2017; 63:843–854.

[2] Başbuğ S, Papadakis G, Vassilicos JC. DNS investigation of the dynamical behaviour of trailing vortices in unbaffled stirred vessels at transitional Reynolds numbers. *Physics of Fluids*. 2017;29:064101.

[3] Gomes-Fernandes R, Ganapathisubramani B, Vassilicos JC. Particle image velocimetry study of fractal-generated turbulence. *Journal of Fluid Mechanics*. 2012;711:306–336.

[4] Nedić J, Vassilicos JC, Ganapathisubramani B. Axisymmetric turbulent wakes with new nonequilibrium similarity scalings. *Physical Review Letters*. 2013;111:1–5.

[5] Weitemeyer S, Reinke N, Peinke J, Hölling M. Multi-scale generation of turbulence with fractal grids and an active grid. *Fluid Dynamics Research*. 2013;45:061407.

[6] Nagata K, Sakai Y, Inaba T, Suzuki H, Terashima O, Suzuki H. Turbulence structure and turbulence kinetic energy transport in multiscale/fractal-generated turbulence. *Physics of Fluids*. 2013;25:065102.

[7] Zhou Y, Nagata K, Sakai Y, Suzuki H, Ito Y, Terashima O, Hayase T. Relevance of turbulence behind the single square grid to turbulence generated by regular- and multiscale-grids. *Physics of Fluids*. 2014;26:075105.

[8] Dairay T, Obligado M, Vassilicos JC. Non-equilibrium scaling laws in axisymmetric turbulent wakes. *Journal of Fluid Mechanics*. 2015;781:166–195.

[9] Nedić J, Ganapathisubramani B, Vassilicos JC, Borée J, Brizzi LE, Spohn A. Aeroacoustic Performance of Fractal Spoilers. *AIAA Journal*. 2012;50:2695–2710.

[10] Nedić J, Vassilicos JC. Vortex shedding and aerodynamic performance of an airfoil with multiscale trailing-edge modifications. *AIAA Journal*. 2015;53:3240–3250.

[11] Melina G, Bruce PJK, Vassilicos JC. Vortex shedding effects in grid-generated turbulence. *Physical Review Fluids*. 2016;1:044402.

[12] Nedić J, Supponen O, Ganapathisubramani B, Vassilicos JC. Geometrical influence on vortex shedding in turbulent axisymmetric wakes. *Physics of Fluids*. 2015;27:035103.

[13] Cafiero G, Discetti S, Astarita T. Heat transfer enhancement of impinging jets with fractal-generated turbulence. *International Journal of Heat and Mass Transfer*. 2014; 75:173–183.

[14] Goh KHH, Geipel P, Hampp F, Lindstedt RP. Flames in fractal grid generated turbulence. *Fluid Dynamics Research*. 2013;45:061403.

[15] Soulopoulos N, Kerl J, Sponfeldner T, Beyrau F, Hardalupas Y, Taylor AMKP, Vassilicos JC. Turbulent premixed flames on fractal-grid-generated turbulence. *Fluid Dynamics Research*. 2013;45:061404.

[16] Goh K, Geipel P, Lindstedt R. Lean premixed opposed jet flames in fractal grid generated multiscale turbulence. *Combustion and Flame*. 2014;161:2419–2434.

[17] Suzuki H, Nagata K, Sakai Y, Ukai R. High-Schmidt-number scalar transfer in regular and fractal grid turbulence. *Physica Scripta*. 2010;T142:014069.

[18] Suzuki H, Nagata K, Sakai Y, Hayase T. Direct numerical simulation of turbulent mixing in regular and fractal grid turbulence. *Physica Scripta*. 2010;T142:014065.

[19] Laizet S, Vassilicos JC. Fractal space-scale unfolding mechanism for energy-efficient turbulent mixing. *Physical Review E*. 2012;86:1–5.

[20] Laizet S, Vassilicos JC. Stirring and scalar transfer by grid-generated turbulence in the presence of a mean scalar gradient. *Journal of Fluid Mechanics*. 2015;764:52–75.

[21] Nienow AW. Stirring and stirred-tank reactors. *Chemie-Ingenieur-Technik*. 2014; 86:2063–2074.

[22] Nedić J, Ganapathisubramani B, Vassilicos JC. Drag and near wake characteristics of flat plates normal to the flow with fractal edge geometries. *Fluid Dynamics Research*. 2013;45:061406.

[23] Başbuğ S, Papadakis G, Vassilicos J. Reduced power consumption in stirred vessels by means of fractal impellers. *AIChE Journal*. 2018; 64:1485-1499.

[24] Paul EL, Kresta SM, Atiemo-Obeng VA. *Handbook of Industrial Mixing: Science and Practice*. Hoboken, NJ, USA: John Wiley & Sons, Inc. 2004.

[25] Aref H. Stirring by chaotic advection. *Journal of Fluid Mechanics*. 1984;143:1–21.

[26] Southerland KB, Frederiksen RD, Dahm WJA, Dowling DR. Comparisons of mixing in chaotic and turbulent flows. *Chaos, Solitons and Fractals*. 1994;4:1057–1089.

[27] Dopazo C, Calvo P, Pétriz F. A geometric/kinematic interpretation of scalar mixing. *Physics of Fluids*. 1999;11:2952–2956.

[28] Toussaint V, Carriere P, Scott J, Gence JN. Spectral decay of a passive scalar in chaotic mixing. *Physics of Fluids*. 2000;12:2834–2844.

[29] Warhaft Z. Passive Scalars in Turbulent Flows. *Annual Review of Fluid Mechanics*. 2000;32:203–240.

[30] Pope SB. *Turbulent Flows*. Cambridge University Press, United Kingdom. 2000.

[31] Kukukova A, Aubin J, Kresta SM. A new definition of mixing and segregation: Three dimensions of a key process variable. *Chemical Engineering Research and Design*. 2009; 87:633–647.

[32] Nagata S. *Mixing: Principles and applications*. New York: Wiley. 1975.

[33] Nienow AW. On impeller circulation and mixing effectiveness in the turbulent flow regime. *Chemical Engineering Science*. 1997;52:2557–2565.

[34] Yoon HS, Hill DF, Balachandar S, Adrian RJ, Ha MY, Balachandar, Adrian RJ, Ha SMY. Reynolds number scaling of flow in a Rushton turbine stirred tank. Part I - Mean flow, circular jet and tip vortex scaling. *Chem Eng Sci*. 2005;60:3169–3183.

[35] Raju R, Balachandar S, Hill DF, Adrian RJ. Reynolds number scaling of flow in a stirred tank with Rushton turbine. Part II - Eigen decomposition of fluctuation. *Chemical Engineering Science*. 2005;60:3185–3198.

[36] Kramers H, Baars G, Knoll W. A comparative study on the rate of mixing in stirred tanks. *Chemical Engineering Science*. 1953;2:35–42.

[37] Hoogendoorn C, den Hartog A. Model studies on mixers in the viscous flow region. *Chemical Engineering Science*. 1967;22:1689–1699.

[38] Moo-Young M, Tichar K, Dullien FAL. The blending efficiencies of some impellers in batch mixing. *AIChE Journal*. 1972;18:178–182.

[39] Khang SJ, Levenspiel O. New scale-up and design method for stirrer agitated batch mixing vessels. *Chemical Engineering Science*. 1976;31:569–577.

[40] Grenville R. Blending of viscous Newtonian and pseudo-plastic fluids. Ph.D. thesis, Cranfield Institute of Technology, England. 1992.

[41] Distelhoff MFW, Marquis AJ, Nouri JM, Whitelaw JH. Scalar mixing measurements in batch operated stirred tanks. *The Canadian Journal of Chemical Engineering*. 1997; 75:641–652.

[42] Rousseaux JM, Muhr H, Plasari E. Mixing and micromixing times in the forced vortex region of unbaffled mixing devices. *The Canadian Journal of Chemical Engineering*. 2001;79:697–707.

[43] Assirelli M, Bujalski W, Eaglesham A, Nienow AW. Macro- and micromixing studies in an unbaffled vessel agitated by a Rushton turbine. *Chemical Engineering Science*. 2008;63:35–46.

[44] Cabaret F, Fradette L, Tanguy PA. New turbine impellers for viscous mixing. *Chemical Engineering and Technology*. 2008;31:1806–1815.

[45] Murthy Shekhar S, Jayanti S. CFD Study of Power and Mixing Time for Paddle Mixing in Unbaffled Vessels. *Chemical Engineering Research and Design*. 2002;80:482–498.

[46] Bujalski J, Jaworski Z, Bujalski W, Nienow A. The Influence of the Addition Position of a Tracer on CFD Simulated Mixing Times in a Vessel Agitated by a Rushton Turbine. *Chemical Engineering Research and Design*. 2002;80:824–831.

[47] Montante G, Mostek M, Jahoda M, Magelli F. CFD simulations and experimental validation of homogenisation curves and mixing time in stirred Newtonian and pseudoplastic liquids. *Chemical Engineering Science*. 2005;60:2427–2437.

[48] Jahoda M, Tomášková L, Moštěk M. CFD prediction of liquid homogenisation in a gas-liquid stirred tank. *Chemical Engineering Research and Design*. 2009;87:460–467.

[49] Coroneo M, Montante G, Paglianti A, Magelli F. CFD prediction of fluid flow and mixing in stirred tanks: Numerical issues about the RANS simulations. *Computers and Chemical Engineering*. 2011;35:1959–1968.

[50] Yeoh SL, Papadakis G, Yianneskis M. Determination of mixing time and degree of homogeneity in stirred vessels with large eddy simulation. *Chemical Engineering Science*. 2005;60:2293–2302.

[51] Hartmann H, Derksen JJ, Van den Akker HEA. Mixing times in a turbulent stirred tank by means of LES. *AIChE Journal*. 2006;52:3696–3706.

[52] Zadghaffari R, Moghaddas JS, Revstedt J. A mixing study in a double-Rushton stirred tank. *Computers and Chemical Engineering*. 2009;33:1240–1246.

[53] Roy S, Acharya S. Scalar mixing in a turbulent stirred tank with pitched blade turbine: Role of impeller speed perturbation. *Chemical Engineering Research and Design*. 2012; 90:884–898.

[54] Yang F, Zhou S, Wang G. Detached eddy simulation of the liquid mixing in stirred tanks. *Computers and Fluids*. 2012;64:74–82.

[55] Ruszkowski S. A Rational Method for Measuring Blending Performance, and Comparison of Different Impeller Types. In: *Proceedings of the 8th European conference on mixing*. Cambridge, U.K. 1994; pp. 283–291.

[56] Derksen JJ. Blending of miscible liquids with different densities starting from a stratified state. *Computers and Fluids*. 2011;50:35–45.

[57] Nisancioglu K, Newman J. Diffusion in aqueous nitric acid solutions. *AIChE Journal*. 1973;19:797–801.

[58] Eggels JGM. Direct and large-eddy simulation of turbulent fluid flow using the lattice-Boltzmann scheme. *International Journal of Heat and Fluid Flow*. 1996;17:307–323.

[59] Derksen JJ, Van den Akker HEA. Parallel simulation of turbulent fluid flow in a mixing tank. *High-Performance Computing and Networking*. 1998;1401:96–104.

[60] Derksen JJ, Van den Akker HEA. Large eddy simulations on the flow driven by a Rushton turbine. *AIChE Journal*. 1999;45:209–221.

[61] Derksen JJ. Direct simulations of mixing of liquids with density and viscosity differences. *Industrial and Engineering Chemistry Research*. 2012;51:6948–6957.

[62] Yeoh SL, Papadakis G, Yianneskis M. Numerical simulation of turbulent flow characteristics in a stirred vessel using the LES and RANS approaches with the sliding/deforming mesh methodology. *Chemical Engineering Research and Design*. 2004; 82:834–848.

[63] Thomareis N, Papadakis G. Effect of trailing edge shape on the separated flow characteristics around an airfoil at low Reynolds number: A numerical study. *Physics of Fluids*. 2017;29:014101.

[64] Paul I, Papadakis G, Vassilicos JC. Genesis and evolution of velocity gradients in near-field spatially developing turbulence. *Journal of Fluid Mechanics*. 2017;815:295–332.

[65] Assirelli M, Bujalski W, Eaglesham A, Nienow AW. Intensifying micromixing in a semi-batch reactor using a Rushton turbine. *Chemical Engineering Science*. 2005; 60:2333–2339.

[66] Ducci A, Yianneskis M. Vortex tracking and mixing enhancement in stirred processes. *AIChE Journal*. 2007;53:305–315.

[67] Doulgerakis Z, Yianneskis M, Ducci A. On the interaction of trailing and macro-instability vortices in a stirred vessel-enhanced energy levels and improved mixing potential. *Chemical Engineering Research and Design*. 2009;87:412–420.

[68] Vassilicos JC. Mixing in vortical, chaotic and turbulent flows. *Philosophical Transactions of the Royal Society A: Mathematical, Physical and Engineering Sciences*. 2002; 360:2819–2837.